



Graphene-decorated 3D BiVO₄ superstructure: Highly reactive (040) facets formation and enhanced visible-light-induced photocatalytic oxidation of NO in gas phase

Man Ou ^{a,b}, Qin Zhong ^{a,b,*}, Shule Zhang ^{a,b}, Haoyu Nie ^{a,b}, Zijian Lv ^{a,b}, Wei Cai ^{a,b}

^a School of Chemical Engineering, Nanjing University of Science and Technology, Nanjing, Jiangsu 210094, PR China

^b Nanjing AIREP Environmental Protection Technology Co., Ltd., Nanjing, Jiangsu 210091, PR China

ARTICLE INFO

Article history:

Received 21 February 2016

Received in revised form 10 April 2016

Accepted 14 April 2016

Available online 22 April 2016

Keywords:

3D BiVO₄

Graphene

(040) facets

PCO

NO

ABSTRACT

In this study, graphene-decorated 3D flower-like BiVO₄ photocatalyst coupling with highly reactive (040) facets was synthesized by a facile alkaline solvothermal route. With the addition of graphene oxide (GO), the size of the subunits composing the 3D flower-like dramatically decreases, while the size of the flower is almost unchanged. Fascinatingly, the introduction of GO in the synthesis medium facilitates the preferential crystal growth of the 3D BiVO₄ photocatalyst along its (040) facets. The as-prepared 3D BiVO₄/graphene composites with the exposed (040) facets exhibits the enhanced activity in the visible-light photocatalytic oxidation (PCO) of NO (~400 ppm), wherein the BiVO₄/graphene (2.4 wt%) composite displays the highest photoactivity of PCO of NO. The improved photocatalytic performance was found to be associated with the synergistic effects of the exposed photogenerated electron-rich (040) facets of BiVO₄ and the enhanced electronic conductivity caused by the graphene, and more significantly, the interaction between BiVO₄ and graphene sheets which reduces the recombination of photoinduced charge carriers. The present study points out that the role of graphene is not only a capping agent to design the highly reactive (040) facets, but also a catalyst promoter for the photocatalytic performance, resulting in an enhanced photoactivity.

© 2016 Elsevier B.V. All rights reserved.

1. Introduction

Semiconductor photocatalysts, which could efficiently and environmental friendly alleviate the deterioration of natural environments created by air and water pollutions, have been received keen interest in recent years. Traditional photocatalyst TiO₂ shows its remarkable ability in the photocatalytic fields like energy conversion, water splitting to hydrogen and NO degradation [1–3]. However, it has a wide energy band of 3.2 eV and can only work under the UV-light ($\lambda < 388$ nm) radiation. This would limit its photocatalytic application in the visible light region, the main part (43%) of solar spectrum [4,5]. In consideration of the efficient utilization of solar light, the preparation and application of a visible-light-activated photocatalyst, which will give activities as good as TiO₂ under UV irradiation, could be favorable.

Monoclinic BiVO₄ (ms-BiVO₄), an attractive visible-light-response semiconductor material, has been extensively investigated and applied in the photocatalytic field due to its relatively narrow band gap (~2.4 eV), excellent chemical stability, nontoxicity, and low cost [6,7]. The semiconductor with a positive valence band value ($E_{VB} = 2.76$ eV) appears to be a promising candidate for photocatalytic oxidation of NO (E_0 (HNO₃/NO) = 0.94 eV) under visible light irradiation [8–10]. Theoretical and experimental studies have demonstrated that the ms-BiVO₄ photocatalyst with the predominately exposed (040) facets is efficient in boosting the photocatalytic performance [11]. The reason is that the photogenerated electron-rich (040) facets provide more multi-atomic centers BiV₄, which is the origin of the multi-electron transfer involved in the photocatalytic reaction [11,12]. Indeed, some researchers have demonstrated that an increase in the (040) crystal facet of ms-BiVO₄ has a significant influence on the photocatalytic performance. The sheet-like BiVO₄ material displaying a preferred (040) surface orientation using TiCl₃ as the directing agent demonstrated excellent visible-light photocatalytic activity for O₂ evolution [11]. Recently, a green method has been developed for the fabrication of ms-BiVO₄ with the preferentially

* Corresponding author at: School of Chemical Engineering, Nanjing University of Science and Technology, Nanjing, Jiangsu 210094, PR China.

E-mail address: zq304@mail.njust.edu.cn (Q. Zhong).

exposed reactive (040) facets using ammonium carbonate as the structure-directing agent, where an enhancement in the photocatalytic oxidation of ethylene was observed under visible light irradiation [13]. However, the photocatalytic performance of pure ms-BiVO₄ is still limited by its poor charge carriers transport property.

Coupling with graphene, an excellent electron transfer property with a charge transfer mobility of 200,000 cm² V⁻¹ s⁻¹, has been considered as a promising method to meet the challenge [14,15]. Furthermore, the unique high specific surface area (2600 m² g⁻¹) plane structure, coupled with its excellent electronic, mechanical, chemically stable features, makes graphene sheets a supporting platform for the deposition and stabilization semiconductors to produce the highly dispersed composite catalysts [16]. Recently, several studies have clearly demonstrated the improvement of the photocatalytic performance of ms-BiVO₄ with the addition of graphene. For instance, Sun and co-workers fabricated three-dimensional acicular sheaf shaped BiVO₄/reduced graphene oxide composites, which showed enormous enhanced photocatalytic activity for the degradation of RhB under visible light irradiation [17]. Fu et al. synthesized BiVO₄-graphene composites with high catalytic performance in photocatalytic dyes by a hydrothermal route [8]. The excellent photocatalytic performance was mainly attributed to the enhancement of the separation and transfer of photo-induced carriers due to the interaction between BiVO₄ and graphene. However, the variation of facets or morphology of ms-BiVO₄ caused by the interfacial interaction between ms-BiVO₄ and graphene sheets have seldom been reported. The presence of oxygen functionalities at GO could allow it to confine the cations on the surface, subsequently providing reactive sites for the nucleation and controlled crystal growth for the semiconductor [18–20].

Herein, the feasible alkaline solvothermal treatment was conducted to fabricate the 3D flower-like ms-BiVO₄/reduced graphene oxide nanosheets (ms-BiVO₄/rGONS) composites with the highly exposed (040) facets. The strong interaction between the (040) facets of BiVO₄ and rGONS surface in the obtained composite photocatalysts was characterized by several techniques. A high concentration of NO (~400 ppm) was used for the PCO activity, which adopted the 3D BiVO₄/rGONS as the photocatalyst. The enhanced ability of the PCO of NO was remarkable, and reasons were discussed. As well, in this paper, the effect of active species on the enhanced photoactivity over 3D BiVO₄/rGONS photocatalyst was also clarified.

2. Experimental

2.1. Preparation of 3D BiVO₄/rGONS

All the chemicals were reagent-grade and used without further purification. Here, GO was prepared from natural graphite powder using Hummers method as mentioned in our previous paper [21]. 40 mg GO powder was added into 100 mL ethylene glycol solution, and then the mixture was ultrasonicated for 2 h to make the brown homogeneous GO nanosheets suspension.

The BVO-rGONS composites were synthesized via a facile solvothermal method using Bi(NO₃)₃·5H₂O, NH₄VO₃, and exfoliated GO nanosheets as the precursor. In a typical synthesis, 0.485 g Bi(NO₃)₃·5H₂O was well dispersed into a certain amount of GO suspension under vigorous stirring, to which certain ethylene glycol solution was added to reach the amount of 40 mL. Meanwhile 0.117 g NH₄VO₃ was dissolved in 40 mL 80 °C distilled water with mechanical agitation to form a transparent solution, and then added dropwise into the obtained mixture afterwards and the pH value was adjusted to about 8 by the NH₃·H₂O. After being stirred for 30 min, the precursor solution was consequently transferred

into a 100 mL Teflon-lined stainless steel autoclave and maintained at 180 °C and autogenous pressure for 15 h. After the autoclave was cooled down to room temperature, the dark-green precipitation was collected by centrifugation, washed by distilled water and absolute alcohol for several times, and then dried in a vacuum oven at 80 °C overnight. The obtained BiVO₄-reduced graphene oxide nanosheet samples prepared with 10, 20 and 30 mL GO suspension were labeled as BVO/rGONS-10 (1.2 wt%), BVO/rGONS-20 (2.4 wt%) and BVO/rGONS-30 (3.6 wt%). For comparison, same method was used to synthesize pure luminous yellow BiVO₄ (BVO) sample without GO, in which 0.485 g Bi(NO₃)₃·5H₂O and 0.117 g NH₄VO₃ was dissolved in 40 mL ethylene glycol solution and 40 mL 80 °C distilled water, respectively, and the remaining experimental parameters were the same as that of BVO-rGONS composites.

2.2. Characterizations

The structural and chemical information for prepared samples were measured by X-ray diffraction (XRD, Cu K α , Purkinje XD-3), Field-emission scanning electron microscope (SEM, FEI Quanta 250F), Raman spectra (Renishaw (in Via)), X-ray photoelectron spectroscopy (XPS, PHI-5000C ESCA), UV-vis diffuse reflectance spectra (DRS, Shimadzu UV-2600), Photoluminescence spectra (PL, He-Cd laser, Labram-HR800). Produced ions in the solution were analyzed by Ion Chromatography (IC, Dionex ICS90).

2.3. The photocatalytic reaction

The experiments for the photocatalytic oxidation (PCO) of NO were conducted at room temperature and atmospheric pressure in a fixed bed continuous flow tubular quartz reactor ($d = 1$ cm, $h = 15$ cm). The 350 W Xe-lamp was vertically placed, parallel with the reactor and a 420 nm cut-off filter was also placed. Photocatalyst (0.2 g) was carefully deposited on the inner walls of the reactor from a suspension of finely ground power in distilled water. After deposition, the reactor was dried at 100 °C overnight to remove the water. Also, a small piece of clean cotton was placed at the bottom of the reactor. After the PCO of NO experiments, little photocatalyst power was found on the cotton, which demonstrated that the layer of the photocatalyst had a desirable resistance to the air flow and the small flow of the H₂O₂ solution. The mixture of reactant gases (400 ppm NO, 7% O₂/N₂ balance) was fed into the reactor with a total flow rate of 100 mL min⁻¹. In order to provide more active species for the PCO of NO and reduce the accumulation of reaction products on the surface of photocatalysts, 30% H₂O₂ solution was injected into the reactor with a flow rate of 0.02 mL min⁻¹. After the system was stable for 60 min, when there was no difference between the concentration of outlet NO and that of inlet gas, the lamp was turned on and the experiment started. The gas products (every 10 min reaction) were analyzed by an Ecom-JZKN flue gas analyzer (Germany) for 150 min under visible-light irradiation. The reaction of NO with O₂ was ignorable. The NO conversion is defined as:

$$\text{NO conversion} = (\text{NO}_{\text{in}} - \text{NO}_{\text{out}})/\text{NO}_{\text{in}} \times 100\%$$

2.4. Detection of hydroxyl radicals

The formation of hydroxyl radicals (•OH) in the visible light/BVO-rGONS/H₂O₂ system was detected by the fluorescence technique using terephthalic acid (TA) as a probe molecular. The brief experimental procedures were as follows: four quartz tubes, filled with 40 mL aqueous solution containing 0.3 mmol TA and 50 μL 30% H₂O₂ solution at room temperature, were divided into the experimental group (A–C) and the control group (D). Then

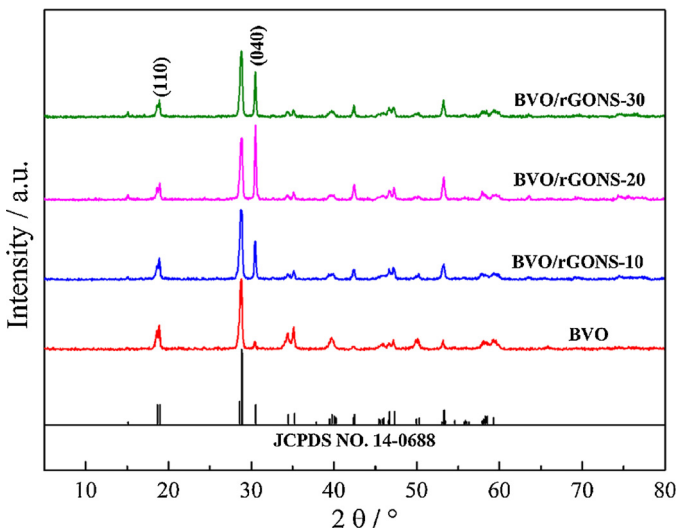


Fig. 1. XRD patterns of pure BVO and BVO/rGONS composites with different content of rGONS. The reference pattern of monoclinic BVO (JCPDS NO. 14-0688) is shown at the bottom.

10 mg BVO/rGONS-20 was dispersed into the experimental group, respectively. Subsequently, all tubes were put under visible-light irradiation in stirring condition for different time, in which A is for 50 min, B is for 100 min, C and D is for 150 min. After the reaction, the clear supernatant was obtained by centrifugation, and •OH in the solution was measured by a FL3-TCSPC fluorescence spectrophotometer.

3. Results and discussion

3.1. Structural and chemical characterizations

Fig. 1 shows the XRD patterns of pure BVO and BVO/rGONS composites. It is found that the position of the diffraction peaks of BVO/rGONS composites is in good agreement with pure BiVO_4 , and they can be well-indexed as the standard monoclinic BiVO_4 (JCPDS NO. 14-0688) [22,23]. This, therefore, indicates that the crystalline and structure of BiVO_4 in the composites do not change and no other impurities are observed. The main difference in the observed patterns pertains to the intensity of the (040) peak. Notably, after coupling with GO, the diffraction peaks corresponding to the (040) of BVO is much higher than that in pure BVO. The intensity of the (040) diffraction peak reaches the maximum in the BVO/rGONS-20 sample. The preferential orientation of the (040) lattice planes in the composites clearly suggests that the addition of GO facilitates the growth of the (040) facets in alkaline ethylene glycol solution. To reveal the variation process of the diffraction peaks of BVO in BVO/rGONS composites, the BVO/rGONS-20 samples of different hydrothermal times were also prepared, as depicted in Fig. S1. It is interesting that the (040) peak corresponding to the monoclinic BVO becomes stronger as the hydrothermal time prolongs. The above results suggested that the addition of GO favors the expression of (040) crystal facets in BVO/rGONS system. Generally, rGONS exhibits the typical diffraction peaks at $2\theta = 26^\circ$ and 44° [24,25]. No above characteristic peak of rGONS in composites is detected. The reason may be due to the low amount of rGONS and its relatively low diffraction intensity in composites.

To visually investigate the influence of the addition of GO on the morphology of BVO particles, the SEM images of the BVO/rGONS composites along with the bare BVO are conducted, as shown in **Fig. 2**. For both pure BVO and the BVO/rGONS composites, the BVO particles exhibit well-fined flower-like 3D superstructure. The

whole flower possesses a 3D eight-pot-shaped structure with high symmetry, which is confirmed by the clear axial lines of the petals. As we previously reported, the 3D BVO superstructure is composed of the subunits. In the synthesis process of 3D BVO superstructure, the smooth subunits are closely attacked one by one, and then form the unique premature flower-like structure. Subsequently, the open space between the pots of the premature BVO superstructure is gradually filled with the subunits, and finally the mature 3D BVO morphology is obtained [26]. The typical SEM images in Fig. S2 clearly display the morphology of rGONS possessing the two-dimensional crumpled layered structure. **Fig. 2b₁–d₁** displays the SEM observation of BVO/rGONS composites, where the rGONS is retained in the form of layered structure (marked by red circles) despite the low dosages. For a closer observation from the magnified SEM image shown in **Fig. 2a₂–d₂**, it can be seen that the subunits size dramatically decreases with the addition of GO, and the subunits structure varies from micro-sized large blocks to small nano-slices. It is documented that the two-dimensional graphene segments contains various oxygen-containing groups, which are always employed as capping agent in the synthesis process of morphology-controlled samples [20]. Based on these characteristics of GO, we suggest that the generated BVO could be capped by GO during the synthesis process of BVO/rGONS composites, stunting the further growth of the subunits and thus leading to a smaller size. Then, the slice subunits combine into the flower-like structure and the size of the flower is almost the same as that of pure BVO. In addition, the thickness of the subunits slices decreases first and then increases with the increase of GO content. It reaches the minimum when the content of GO increases to 2.4 wt%. The subsequent increase of the size is due to the agglomerate of the subunits. Notably, the 3D BVO/rGONS-20 superstructure with the thinnest subunits possesses the strongest (040) peak intensity. The exaltation of the (040) induces the subunits to grow along the (040) facet to form the sheet-like structure subunits, as emphasized in our previous reports [26]. Therefore, the variation of the thickness of the slices subunits is caused by the difference of the (040) crystal plane of BVO. Such features seem to be in good agreement with the variation of the (040) peak in the XRD patterns. The capping agents adsorbed on a crystalline facet would reduce the surface free energy, thus inhibiting the growth rates of the specific crystal facet and retaining the highly reactive crystal facet [27]. In our work, the highly exposed (040) facet in composites suggests that the GO capping agents preferentially adsorbs on the (040) facet, reducing the surface energy of the (040) facet and then restraining the growth along the (040) direction. Subsequently, the subunits with dominant (040) facets orderly assemble to flower-like samples. In general, GO binds strongly to the (040) facets of BVO, governing the final shape of the composite samples. However, by increasing the amount of GO, other crystal facets could also be adsorbed on the GO nanosheets resulting in the subunits fuse together, as shown in **Fig. 2d₂**. The above facts suggest that the size and the shape of the as-prepared BVO/rGONS composites could be susceptible when GO is introduced into the synthesis system, the schematic illustration is shown in **Fig. 3**.

Fig. 4 shows the TEM images of pure BVO and BVO/rGONS-20 composite. In **Fig. 4a₁** and **b₁**, it is observed that the subunits size of BVO in BVO/rGONS-20 composite is much smaller than that in pure BVO, which is consistent with the SEM results. Close investigation of the BVO/rGONS-20 sample through the high magnification TEM image in **Fig. S3** suggests that the 3D BVO is freely coated on the rGONS, confirming the formation of BVO/rGONS-20 composite. To further demonstrate the influence of GO on the (040) facet of BVO in BVO/rGONS-20 sample, the HRTEM images of pure BVO and BVO/rGONS-20 composite are conducted, as shown in **Fig. 4a₂** and **b₂**. The fringe spacing of 0.226 nm is clearly observed in **Fig. 4a₂**, which corresponds to the (211) lattice plane of BVO [28]. How-

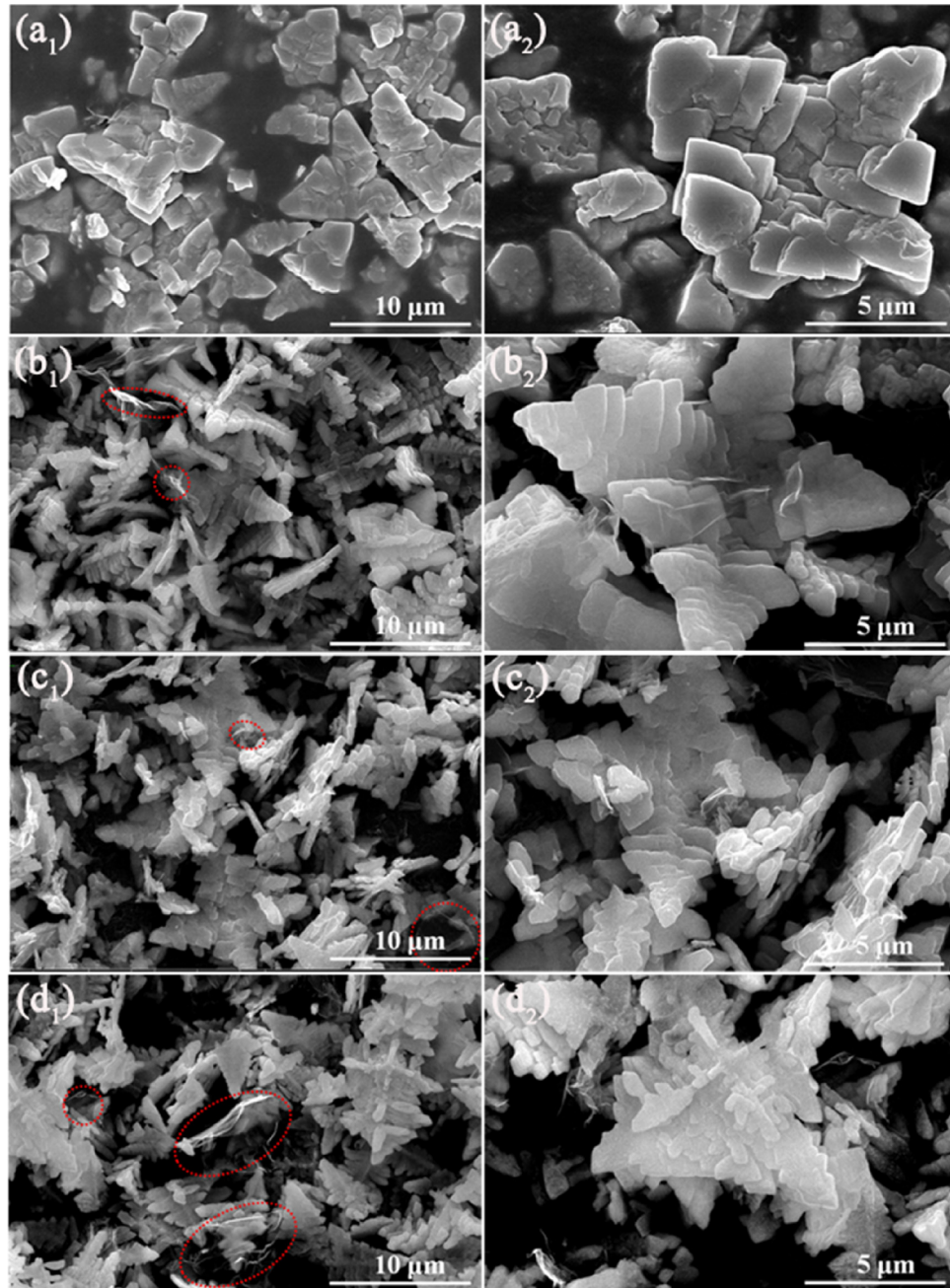


Fig. 2. SEM images of as-synthesized BVO and BVO/rGONS composites with different content of rGONS: BVO (a₁ and a₂); BVO/rGONS-10 (b₁ and b₂); BVO/rGONS-20 (c₁ and c₂) and BVO/rGONS-30 (d₁ and d₂).

ever, for BVO/rGONS-20 composite in Fig. 4b₂, the fringe spacings of 0.261 and 0.255 nm, which agree well with the (200) and (002) lattice planes of BVO, respectively [29]. The angle of 90° between (200) and (002) lattice planes and the corresponding fast Fourier transform (FFT) pattern show that the BVO particles in BVO/rGONS-20 sample grow along the [010] facet. From the results of XRD, SEM and HRTEM, it can be concluded that the growth orientation of BVO in BVO/rGONS-20 composite is along the (040) facet and the GO favors this facet.

Raman spectroscopy can also provide information on the structure of the BVO and the quality of the reduced graphite oxide. Fig. 5 shows the Raman spectra of GO, pure BVO and BVO/rGONS-20 composite. The Raman spectrum of GO contains two bands at 1343 and 1579 cm⁻¹, corresponding to the D-band (the breathing mode of the symmetry A_{1g}) and G-band (the E_{2g} mode of sp² carbon atoms)

[30,31]. However, the D-band shift of GO in the BVO/rGONS-20 composite vanishes and the G-band shift is replaced by a low broad shift peak. It indicates the removal of hydroxyl and epoxy groups and the restoration of sp²-hybridized carbon and thus confirming that the GO is reduced into graphene sheets in the composites during the solvothermal reaction. Compared with the G-band position of GO, the 24 cm⁻¹ shift of the G-band peak to a lower wavenumber could be assigned to an evidence for chemical bonding of carbon materials [32]. In addition, the Raman active peaks at 814 cm⁻¹, 366 cm⁻¹, 325 cm⁻¹ and 196 cm⁻¹ are respectively assigned to the symmetric V–O stretching mode, symmetric and antisymmetric bending modes of the VO₄[−] and an external vibrational mode for the composite, which match well with the monoclinic structure of BVO [33,34]. The results confirm that both the reduction of GO and the formation of pure BVO are achieved simultaneously dur-

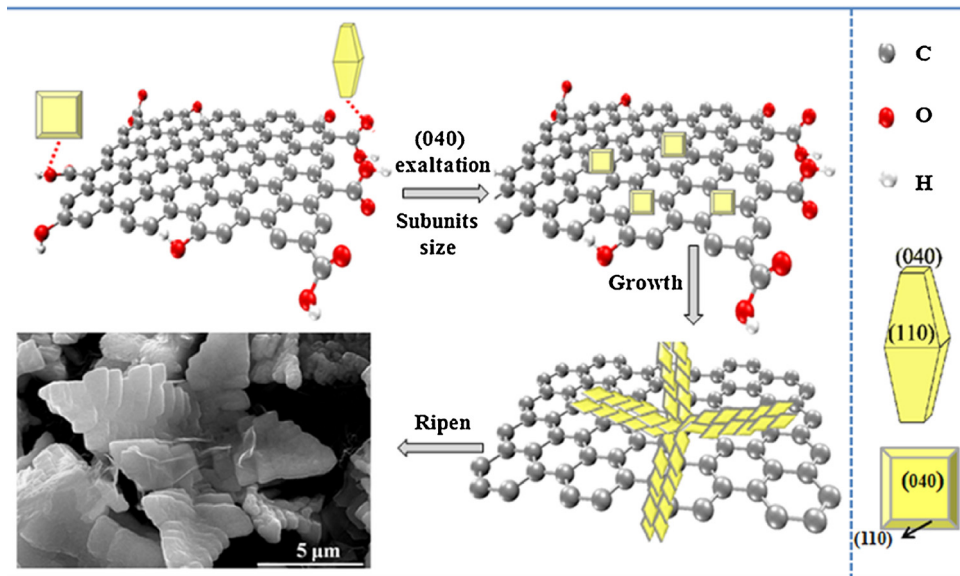


Fig. 3. Schematic illustration of the proposed formation mechanism of 3D flower-like BVO/rGONS superstructure.

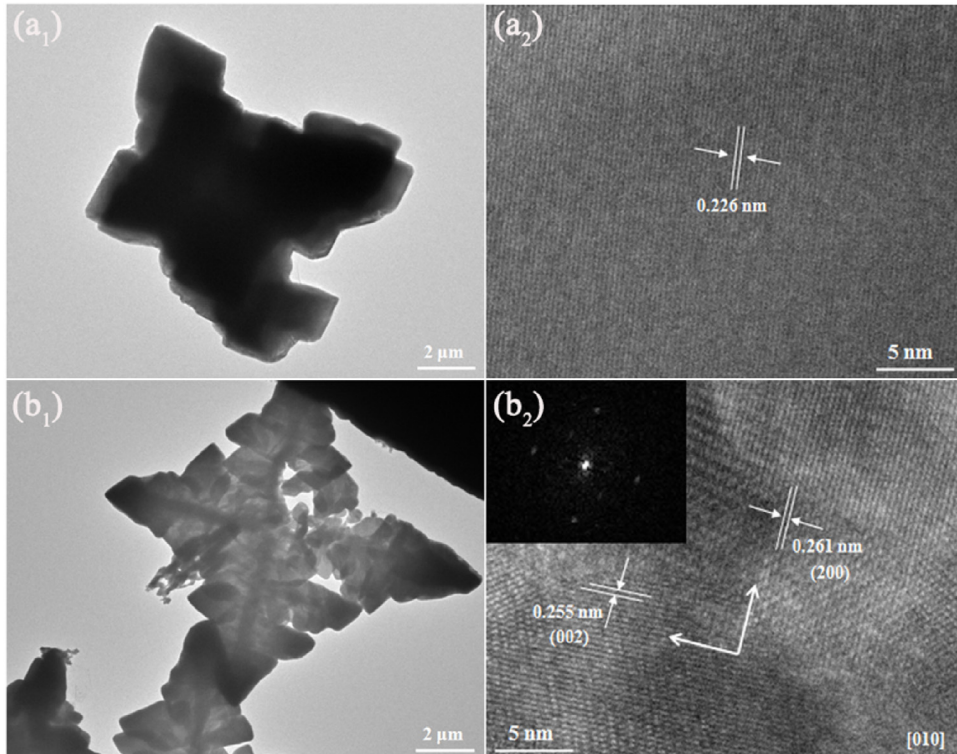


Fig. 4. TEM and HRTEM images of as-synthesized BVO (a₁ and a₂) and BVO/rGONS-20 composite (b₁ and b₂). Inset (b₂) is the corresponding fast Fourier transform (FFT) pattern.

ing the synthesis process of the BVO/rGONS composites in this work, in agreement with XRD analysis. In addition, compared with the primitive BVO, the peak corresponding to the symmetric V–O stretching mode in the composite is broader and the significantly blue-shifts from 829 cm⁻¹ to 814 cm⁻¹ (Fig. 5, inset) is observed. The shift suggests that the composite displays a strong chemical interaction between 3D BVO and rGONS, which is more conducive to the electron transfer to enhance the photoactivity. The similar phenomenon has been observed in the preparation of TiO₂ nanotube/reduced graphene oxide composites [35].

Further evidence for the reduction of GO, the existence of the chemical bonding between 3D BVO and rGONS and the electronic environment after visible light irradiation derives from XPS analysis. Fig. 6 provides the XPS spectra of GO, BVO (A₁), BVO/rGONS-20 composite (A₂) and BVO/rGONS-20 under visible light irradiation for 30 min (A₃). The XPS survey spectra (Fig. S4) display the presence of C, Bi, V and O in both BVO and BVO/rGONS-20 composite. Fig. 6a-d shows the high resolution spectrum of C 1s, Bi 4f, V 2p, and O 1s, respectively. The distinct C 1s XPS spectrum of GO (Fig. 6a) located at ca. 284.6, 286.4, 287, and 288.5 eV, which are attributed to the characteristic peak of graphitic carbon, C–O in hydroxyl

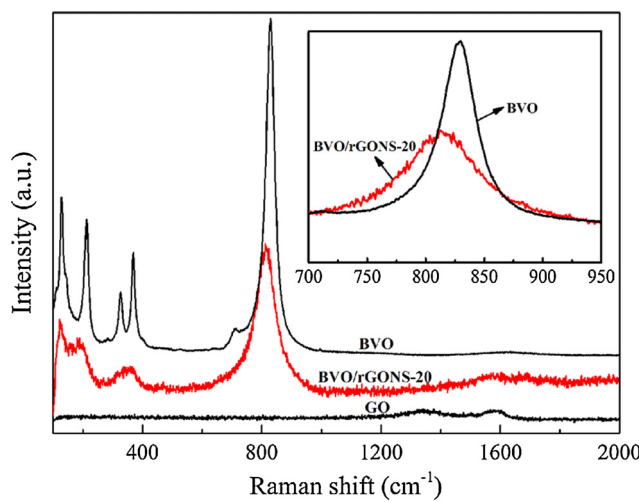


Fig. 5. Raman spectra of GO, BVO and BVO/rGONS-20 samples. Inset: the Raman spectra of the symmetric V—O stretching mode in BVO and BVO/rGONS-20 composite.

or epoxy forms, C=O and O—C=O units of typical GO nanosheets, respectively [36]. However, a great decrease in the relative intensity of the oxygen containing functional groups (C—O, C=O and O—C=O) in BVO/rGONS-20 composite is observed, indicating that graphene exists in the composites instead of GO. Two peaks of pure BVO (Fig. 6b) at 159.1 and 164.5 eV, assigned to Bi 4f_{7/2} and Bi 4f_{5/2}

induced by Bi³⁺ species [37,38], increase to 159.2 and 164.6 eV after the loading of GO. The V 2p shows the peaks at 516.8 and 524.4 eV (Fig. 6c), which are attributed to V⁵⁺ of BVO particles [37,38]. Similarly, the peaks of V 2p in BVO/rGONS-20 composite are also shifted up by 0.1 eV compared with that of pure BVO. For O 1s spectra (Fig. 6d), the peaks at 530 and 531.5 eV, corresponding to the V—O and chemisorbed O—H species on the surface of the BVO [39], shifted to 530.1 and 531.7 eV in the BVO/rGONS composite, respectively. Consequently, compared to that of pure BVO, the banding energies of Bi, V and O in composite shift positively, suggesting the presence of the chemical interaction between BVO and GO. Combined with the XRD and SEM results, we can conclude that during the solvothermal treatment, the functional groups of GO preferentially adsorb onto the (040) surfaces to facilitate the formation of chemical interaction between BVO and GO. Furthermore, the band energies of each element (C, Bi, V and O) in the BVO/rGONS-20 composite under visible light for 30 min shift to the lower band energies compared with that of BVO/rGONS-20. It indicates that the electron density on the surface of BVO/rGONS sample increases under visible light irradiation. For BVO photocatalyst, it is well known that the valence band edge is composed of Bi 6s and O 2p orbitals, while the conduction band edge is contributed by V 3d orbit [8]. The above results illustrate that the valence-band electrons are excited to the conduction band and then transfer to the surface of the composite photocatalyst under visible light irradiation, and subsequently is applied to the photocatalytic reaction.

The optical properties of the as-synthesized BVO sample and their composites are probed with UV-vis diffuse reflection spectra

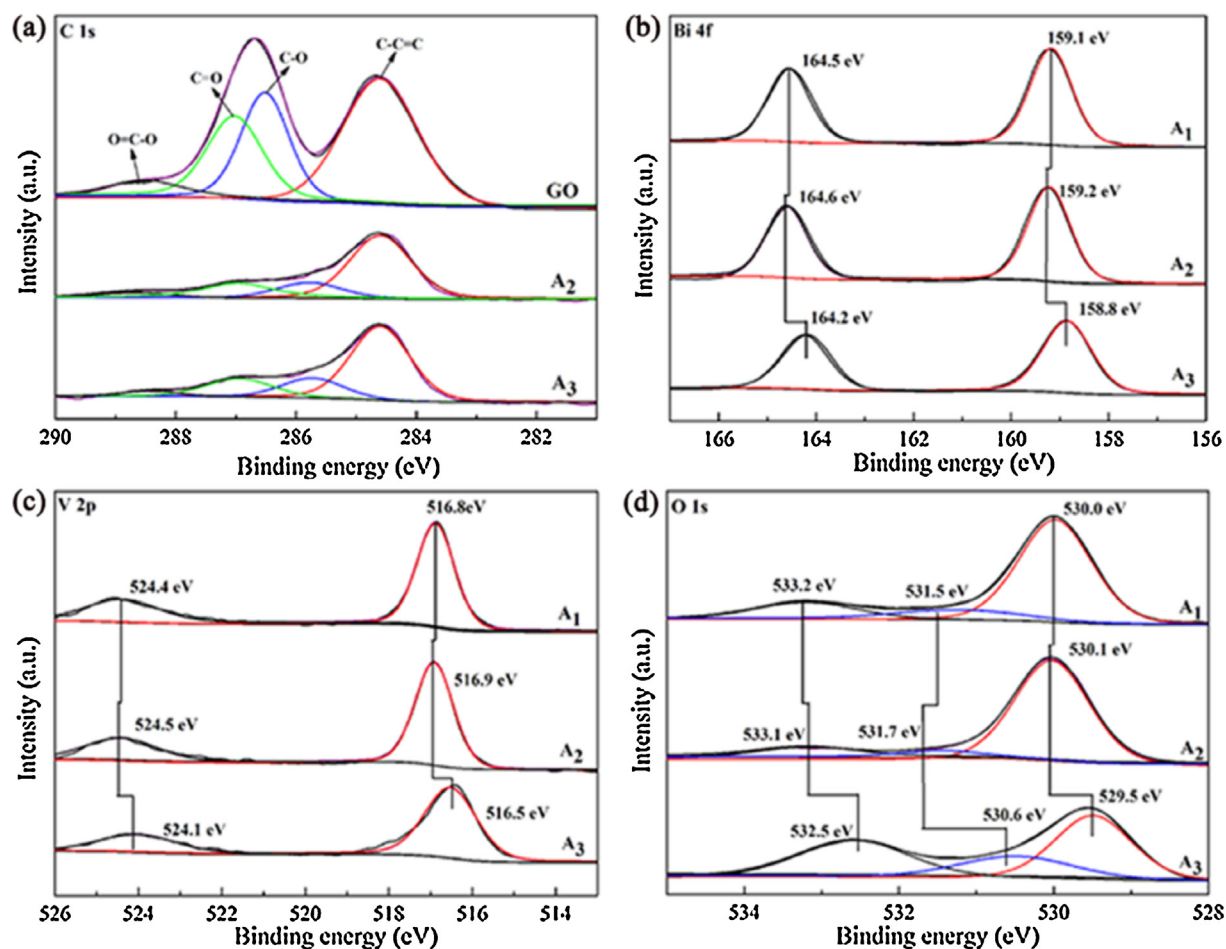


Fig. 6. Comparison of XPS high-resolution scans over C 1s (a), Bi 4f (b), V 2p (c) and O1s (d) peaks on GO, BVO (A₁), BVO/rGONS-20 (A₂) and BVO/rGONS-20 under visible light irradiation for 30 min (A₃).

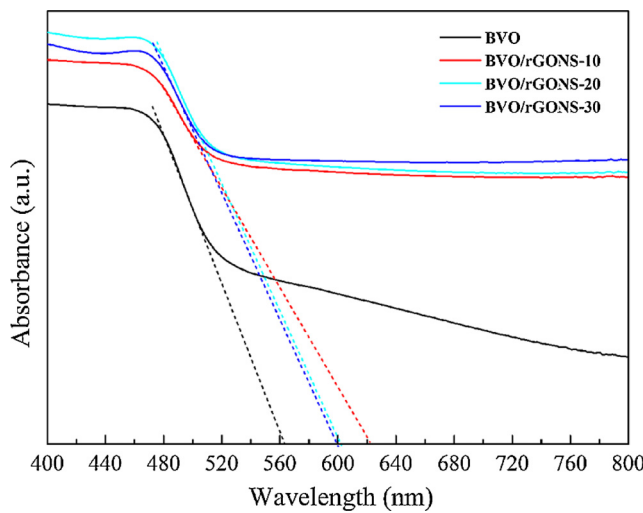


Fig. 7. UV-vis diffuse reflection spectra patterns of the as-synthesized BVO and BVO/rGONS composites with different content of rGONS.

(DRS), as shown in Fig. 7. It can be seen that there is no significant absorption for the 3D BVO in the visible light region, while a wide background absorption covering the whole visible light region is observed for the BVO/rGONS composites. This can be attributed to the fact that the reintroduction of the black body properties of graphite-materials [32]. It is noted that the powder color changes from luminous yellow to dark green after GO addition. In addition, the absorption edge of the composites red-shifts compared with that of pure BVO, which might be ascribed to the interaction between BVO and rGONS during the solvothermal treatment, which is consistent with the results of Raman and XPS analysis. The band gaps (E_g) of BVO and BVO/rGONS composites are assigned as 2.20, 2.00, 2.06 and 2.07 eV respectively, according to the onset of the absorption edge. Among them, the slight variation (0.01 eV) of the E_g value for BVO/rGONS-20 and BVO/rGONS-30 could be negligible. It is clearly that the E_g value of BVO/rGONS composites is obviously smaller than that of pure BVO. And in our case, the photocatalytic performance of BVO/rGONS composites is higher than that of pure 3D BVO. However, the photoactivity of BVO/rGONS composites is inconsistent with the narrow E_g value when GO is introduced in the synthesis system. The BVO/rGONS-10 with narrower E_g value shows lower photocatalytic performance (Part 3.2). The reason for the inconsistency may be that the increased E_g value probably causes a decrease in the valence band edge and an increase in the conduction band edge [40]. This will lead to the reduction of photo-generated carriers recombination rate [40]. We therefore believe the band gap narrowed by the introduction of GO does not contribute to the enhancement of photocatalytic activity of BVO/rGONS composites. Similar results have been reported by some groups [10,41].

3.2. The enhanced photocatalytic activity of NO oxidation

The as-synthesized 3D BVO/rGONS composites with different GO mass ratios are applied on the PCO of NO in gas phase under visible-light irradiation, thus their potential ability for air purification could be basically evaluated. Experimentally, prior to light irradiation, the gas streams were premixed completely and then introduced to a continuous reactor. After the adsorption-desorption equilibrium between gases and photocatalysts was reached, the Xe-lamp and the peristaltic pump that delivers the H₂O₂ solution were turned on. Control experiments indicated that less than 10% NO oxidation ratios was detected in the absence of visible light irradiation, photocatalyst or H₂O₂ solution, illustrating

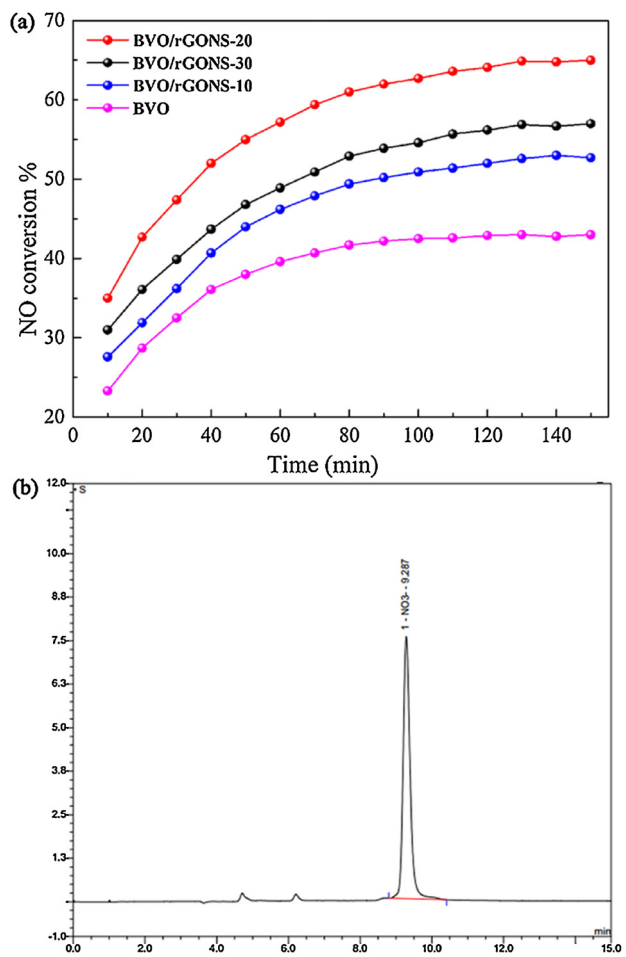


Fig. 8. Variations of NO conversion efficiency with irradiation time for the as-synthesized BVO and BVO/rGONS composites (a); Ion Chromatography analysis of reaction products after the photocatalytic reaction in the presence of BVO/rGONS-20 for 150 min (b).

that NO could hardly be oxidized without photocatalysts, visible-light irradiation and the H₂O₂ solution, or be photolyzed by mere visible-light irradiation. Fig. 8a reveals the variations of NO oxidation efficiency over the different samples. The efficiency of PCO of NO increases gradually with an increasing of GO at the beginning, and then decreases slightly when the GO content is increased to 3.6 wt%. As expected, all of the composites exhibit higher photocatalytic performance than the pristine 3D BVO. In addition, it takes some times longer for the BVO/rGONS to reach kinetic equilibrium, compared to the blank BVO. Through reviewing the PCO experimental procedure, studying relevant information which reported that graphene had great adsorption ability [42], the cause responsible for this phenomenon may be inferred as following: in the PCO experiments, 30% H₂O₂ solution was injected into the quartz reactor with a flow rate of 0.02 mL min⁻¹ by a peristaltic pump. We turned on the peristaltic pump as soon as the Xe-lamp was turned on, which marked the beginning of the PCO reaction. In the initial reaction stage of the PCO experiments, graphene and BVO in BVO/rGONS composites were involved competitive adsorption of H₂O₂. When the BVO/rGONS photocatalyst adsorption saturation with H₂O₂ was reached, the activity of the PCO reaction could become stable and the NO conversion achieved the kinetic equilibrium. The experiment for the PCO of NO was carried out by pure rGONS with the same photocatalytic reaction parameters. From Fig. S5, it could be seen that the activity of the PCO reaction gradually increased and became stable (10%) after 40 min.

In addition, the photoactivity was only 6.7% with the absence of the photocatalyst, which was emphasized in our previous results [26]. Based on the results, it indicated that the PCO of NO of pure rGONS was attributed to the adsorption of H_2O_2 , which generated active species to oxidate NO. When the rGONS adsorption saturation with H_2O_2 was reached, generated active species on the surface of the photocatalyst met the maximum amount, so the activity of the PCO reaction became stable and the NO conversion achieved the steady. Therefore, it could be concluded that it needed some time longer for the BVO/rGONS to reach kinetic equilibrium compared to the blank BVO due to the competitive adsorption of H_2O_2 by rGONS. More specifically, 3D BVO/rGONS-20 with more exposed (040) facets shows the highest NO removal sufficiency (65%). The enhanced photocatalytic performance accords well with its increased (040) facets, as was confirmed by the XRD analysis. It is found that the photogenerated electrons mainly concentrate on the highly exposed (040) facets under the visible light irradiation [11]. The graphene in BVO/rGONS composites can conduct the electrons to accelerate the separation of photogenerated electrons and holes and then to improve the photoactivity. Afterwards, in order to intuitively verify the role of (040) facets on the photocatalytic performance, the 3D BVO/rGONS-20 with different (040) facets at different time was investigated complementary (Fig. S6). With the gradually increased intensity of (040) facets under the condition of the same content of GO, the efficiency of PCO of NO also gradually enhances. This comparison indicates that the photocatalytic performance is dependent on the content of (040) facets. The photocatalysts with exposed (040) facets provide more effective reaction sites for the photocatalytic activity [29]. Therefore, the determining factor for the improvement of the photocatalytic performance is the exposed (040) active sites. This superior PCO of NO of the BVO/rGONS-20 composite could be attributed to the positive synergistic effect between 3D BVO with high (040) facets and rGONS: (i) the interaction between 3D BVO and rGONS induces the generation of the high (040) facets of BVO in composites; (ii) rGONS with the high electrical conductivity could be used as electrons transporters to transfer the carriers transfer; (iii) the high photogenerated electron-rich (040) facets is conducive to the charge separation with the assistance rGONS, which will be proved by PL.

Ion Chromatography (IC) is used to clarify the composition of reaction products of the PCO of NO in the presence of BVO/rGONS photocatalysts under visible-light irradiation, as well as further verify the results of photocatalytic performance. After an experiment was completely conducted, the photocatalyst and the small piece of cotton with ionic liquid that adhered to it was placed in the culture dish ($d=60\text{ mm}$) with the collected solution of reaction products. Furthermore, 10 mL deionized water was added into the mixture and then the culture dish was placed for 120 min in order that ions on the surface of the photocatalyst after reaction could intensively dissolve into the solution. After the clear supernatant was obtained by centrifugation, 2 mL solution was taken out, diluted with deionized water in the ratio of 1:50, and then injected into IC. The result of qualitative analysis, taking BVO/rGONS-20 for an instance, is shown in Fig. 8b, which demonstrated that NO_3^- exists in the solution. In addition, there was no increase of NO_2 in the whole experimental process. And NO_2^- was not detected in the IC. These results could be attributed to the addition of H_2O_2 , which produced considerable amount of active species in the presence of the BVO/rGONS photocatalyst and enhanced the oxidative ability of the system. Therefore, it could be obtained that NO_3^- is the main PCO reaction product, which had been demonstrated in our previous report [43]. The standard solutions were prepared and the corresponding IC was conducted, of which the fitting line is displayed in Fig. S7. Therefore, the concentration of NO_3^- could be acquired by external standard method, which is 11.38, 14.25, 18.52, 15.65 mg L^{-1} , respectively. In order to exclude the influence of material itself, the

content of NO_3^- on the surface of BVO/rGONS-20 photocatalyst is also measured. 0.2 g BVO/rGONS-20 photocatalyst was immersed in 10 mL deionized water for 120 min and then detected by IC. The concentration of NO_3^- on the surface of photocatalyst was very low (1.21 mg L^{-1}) and could be negligible. The material balancing calculation is carried out to investigate the possible byproducts, and the detailed calculate process was given in the supporting information. It could be further illustrated that NO_3^- is the main reaction product in the system of PCO of NO. In addition, this pattern of the measuring data is in excellent accordance with that of the visible-light-induced PCO performance of BVO/rGONS samples on NO oxidation, which confirms the reliability and accuracy of the PCO experimental results.

To investigate the transfer and recombination process of photo-generated charge carriers of the prepared 3D BVO and 3D BVO/rGONS samples, photoluminescence (PL) technique is conducted. A broad PL peak of pure 3D BVO is observed in Fig. 9, which could be ascribed to the radiative recombination process of self-trapped excitation. This is to say, most of the charge carriers quickly recombine on the surface of 3D BVO to produce PL emission. In contrast, the PL intensity of the BVO/rGONS composites in Fig. 9a is significantly reduced after the modification of GO. The decreased PL signal could be regarded as strong evidence for a remarkable decrease of the recombination rate of electron-hole pairs in the photocatalytic reactions. In addition, the PL intensity of the BVO/rGONS-20 for 15 h is lower than that of the BVO/rGONS-20 for 12 h (Fig. 9b), indicating that the electron-hole separation on the surface of the catalysts with photogenerated electron-rich (040) facets is largely enhanced, and thus generating more photoelectrons and holes with the assistance of rGO. We therefore conclude that the enhanced photocatalytic activity of BVO/rGONS composites is mainly attributed to the effective charge carriers transportation and separation arisen from the strong chemical interaction between BVO and rGONS.

3.3. Mechanism analysis of the photocatalytic oxidation of NO

No NO_2 in the outlet gas was detected in the whole stages of the experiment. Combined with the results of IC, it could be obtained that NO_3^- is the major reaction product in the PCO of NO process. The main active species in the PCO of NO process over the BVO/rGONS photocatalysts is determined by a trapping experiment, which could be intuitively investigated the involvement of active radical species in the photocatalytic process, taking BVO/rGONS-20 for an instance. Five quartz tubes filled with 40 mL deionized water and 4 mL 30% H_2O_2 solution were divided into four experimental groups (a-d) and the control group (e). 10 mg BVO/rGONS-20 sample was put into each experimental group, respectively. Subsequently, 1 mL isopropyl alcohol (IPA) was injected into group (b) to quench the hydroxyl radicals ($\bullet OH$), 0.1 mmol *p*-benzoquinone (BQ) as the scavenger of superoxide radicals ($\bullet O_2^-$) was dispersed into group (c) and 0.1 mmol ammonium oxalate (AO) was added into group (d) as holes (h^+) scavenger [44–46]. Then NO was introduced through the gas distributor and all quartz tubes were exposed to VL irradiation in stirring condition for 30 min. After the clear supernatant was obtained by centrifugation and then injected into IC. Quantitative analysis shows that the concentrations of NO_3^- of the experimental group (a)-(d) as well as the control group (e) are 16.52, 4.61, 9.78, 12.26 and 3.13 mg L^{-1} , respectively. It could be seen that $\bullet OH$, $\bullet O_2^-$ and h^+ are the efficient active species in the PCO of NO over the BVO/rGONS-20 photocatalyst. Since the concentration of NO_3^- in group (b), free from the effect of $\bullet OH$, is the lowest among all experimental groups and only a bit higher than that in control group, it is obvious that $\bullet OH$ plays a pivotal role in the PCO of NO. In order to further validate the $\bullet OH$ formed on the surface of BVO/rGONS-20 sample, the photolumines-

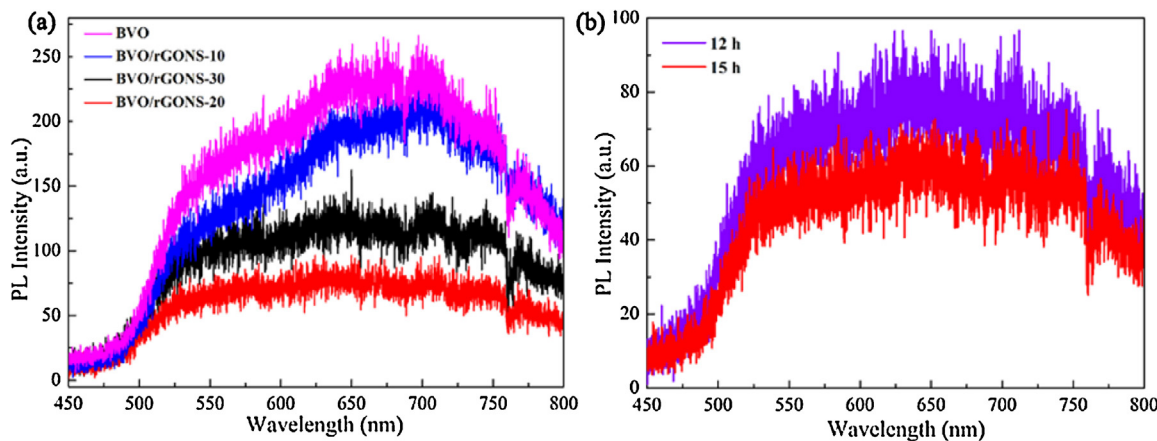


Fig. 9. Photoluminescence spectra of BVO and BVO/rGONS composites with different content of rGONS (a); Photoluminescence spectra of BVO/rGONS-20 at different hydrothermal time (12 h, 15 h) (b).

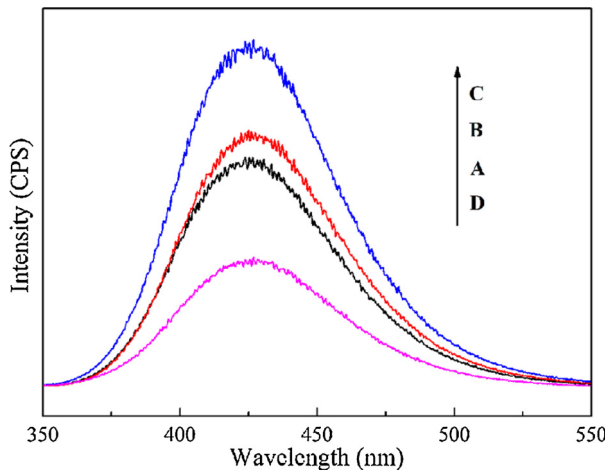


Fig. 10. Fluorescence spectra of TAOH solutions generated by the experimental group with BVO/rGONS-20 for 50 min (A), 100 min (B) and 150 min (C) and the control group for 150 min (D) under visible-light irradiation.

cence (PL) technique using terephthalic acid as a probe molecule was applied. Fig. 10 shows the PL spectra of the control group and the experimental group under different irradiation time (Part 2.4). Obviously, the PL intensity of experimental group (A–C) at about 426 nm is higher than that of the control group (D) and it gradually increased with time. Based on these results, it shows that a large amount of •OH is produced in the presence of BVO/rGONS-20 photocatalyst.

4. Conclusions

In our work, novel flower-shaped BiVO₄ superstructure and graphene-grafted BVO/rGONS composites were fabricated via a solvothermal method. Through this approach, 3D BVO/rGONS composites with the exposed photogenerated electron-rich (040) facets could be formed. Compared with pristine BiVO₄ sample, the composites exhibits both a higher efficiency of PCO of NO and better selectivity for the formation of NO₃⁻. The origin of the distinctly excellent photocatalytic performance of the BVO/rGONS composites could be attributed to the photogenerated electron-rich (040) facets of BVO and interaction of BVO and rGONS. The interaction between BiVO₄ and graphene sheets accelerates the electrons in photogenerated electron-rich (040) facets of BiVO₄ sample preferentially transfer to the graphene efficiently and thus reduces the recombination of photoinduced charge carriers, which is illustrated

by Raman, XPS and PL spectra. Further investigations on mechanism show that •OH plays the dominant role in the PCO of NO through an intuitive trapping experiment and fluorescence spectra.

Acknowledgements

Information Ministry of the People's Republic of China 2012 (543), the National Natural Science Foundation of China (51408309 and 51578288), Science and Technology Support Program of Jiangsu Province (BE2014713), Natural Science Foundation of Jiangsu Province (BK20140777), Industry-Academia Cooperation Innovation Fund Projects of Jiangsu Province (BY2014004-10), Science and technology project of Nanjing (201306012), Jiangsu Province Scientific and Technological Achievements into a Special Fund Project (BA2015062), A Project Funded by the Priority Academic Program Development of Jiangsu Higher Education of Jiangsu Higher Education Institutions.

Appendix A. Supplementary data

Supplementary data associated with this article can be found, in the online version, at <http://dx.doi.org/10.1016/j.apcatb.2016.04.029>.

References

- [1] A. Fujishima, K. Honda, *Nature* 238 (1972) 37–38.
- [2] L.F. Zhang, T.S. Kanki, N. Sano, A. Toyoda, *Sep. Purif. Technol.* 31 (2003) 105–110.
- [3] Z.B. Wu, Z.Y. Sheng, Y. Liu, H.Q. Wang, N. Tang, J. Wang, *J. Hazard. Mater.* 164 (2009) 542–548.
- [4] K.L. Lv, X.F. Li, K.J. Deng, J. Sun, X.H. Li, M. Li, *Appl. Catal. B: Environ.* 95 (2010) 383–392.
- [5] S.J. Hong, S. Lee, J.S. Jang, J.S. Lee, *Energy Environ. Sci.* 4 (2011) 1781–1787.
- [6] L. Zhang, D.R. Chen, X.L. Jiao, *J. Phys. Chem. B* 110 (2006) 2668–2673.
- [7] M.L. Guan, D.K. Ma, S.W. Hu, Y.J. Chen, S.M. Huang, *Inorg. Chem.* 50 (2011) 800–805.
- [8] Y.S. Fu, X.Q. Sun, X. Wang, *Mater. Chem. Phys.* 131 (2011) 325–330.
- [9] M. Ou, Q. Zhong, S.L. Zhang, *J. Sol-Gel Sci. Technol.* 72 (2014) 443–454.
- [10] Z.H. Ai, W.K. Ho, S.C. Lee, *J. Phys. Chem. C* 115 (2011) 25330–25337.
- [11] D. Wang, H.F. Jiang, X. Zong, Q. Xu, Y. Ma, G.L. Li, C. Li, *Chem. Eur. J.* 17 (2011) 1275–1282.
- [12] R.G. Li, H.G. Han, F.X. Zhang, D.E. Wang, C. Li, *Energy Environ. Sci.* 7 (2014) 1369–1376.
- [13] S.M. Thalluri, M. Hussain, G. Saracco, J. Barber, N. Russo, *Ind. Eng. Chem. Res.* 53 (2014) 2640–2646.
- [14] L.H. Huang, K.Y. Hou, X. Jia, H.B. Pan, M. Du, *Mater. Sci. Eng. C* 38 (2014) 39–45.
- [15] H. Hu, Z.B. Zhao, Q. Zhou, Y. Gogotsi, J.S. Qiu, *Carbon* 50 (2012) 3267–3273.
- [16] N. Liu, X.Z. Wang, W.Y. Xu, H. Hu, J.J. Liang, J.S. Qiu, *Fuel* 119 (2014) 163–169.
- [17] S.Y. Dong, Y.R. Cui, Y.F. Wang, Y.K. Li, L.M. Hu, J.Y. Sun, J.H. Sun, *Chem. Eng. J.* 249 (2014) 102–110.

- [18] W.S. Wang, D.H. Wang, W.G. Qu, L.Q. Lu, A.W. Xu, *J. Phys. Chem. C* 116 (2012) 19893–19901.
- [19] Z.X. Song, Y.J. Zhang, W. Liu, S. Zhang, G.C. Liu, H.Y. Chen, J.S. Qiu, *Electrochim. Acta* 112 (2013) 120–126.
- [20] M.S. Zhu, P.L. Chen, M.H. Liu, *Langmuir* 29 (2013) 9259–9268.
- [21] Y.X. Zhao, H.L. Ding, Q. Zhong, *Appl. Surf. Sci.* 258 (2012) 4301–4307.
- [22] L. Ren, L.L. Ma, L. Jin, J.B. Wang, M.Q. Qiu, Y. Yu, *Nanotechnology* 20 (40) (2009) 17579–17584.
- [23] M. Wang, H.Y. Zheng, Q. Liu, C. Niu, Y.S. Che, M.Y. Dang, *Spectrochim. Acta Part A: Mol. Biomol. Spectrosc.* 11 (2013) 74–79.
- [24] Y.F. Dong, Z.B. Zhao, Z.Y. Wang, Y. Liu, X.Z. Wang, J.S. Qiu, *ACS Appl. Mater. Interfaces* 7 (2015) 2444–2451.
- [25] Y.K. Li, S.Y. Dong, Y.F. Wang, J.Y. Sun, Y.F. Li, Y.Q. Pi, L.M. Hu, J.H. Sun, *J. Mol. Catal. A: Chem.* 387 (2014) 138–146.
- [26] M. Ou, H.Y. Nie, Q. Zhong, S.L. Zhang, L. Zhong, *Phys. Chem. Chem. Phys.* 17 (2015) 28809–28817.
- [27] W.J. Ong, L.L. Tan, S.P. Chai, S.T. Yong, A.R. Mohamed, *Nanoscale* 6 (2014) 1946–2008.
- [28] D. Tang, H.C. Zhang, H. Huang, R.H. Liu, Y.Z. Han, Y. Liu, C.Y. Tong, Z.H. Kang, *Dalton Trans.* 42 (2013) 6285–6289.
- [29] D.G. Wang, H.F. Jiang, X. Zong, Q. Xu, Y. Ma, G.L. Li, C. Li, *Chem. Eur. J.* 17 (2011) 1275–1282.
- [30] Y. Yan, S.F. Sun, Y. Song, X. Yan, W.S. Guan, X.X. Liu, W.D. Shi, *J. Hazard. Mater.* 250–251 (2013) 106–114.
- [31] Z.Y. Wang, B.B. Huang, Y. Dai, Y.Y. Liu, X.Y. Zhang, X.Y. Qin, J.P. Wang, Z.K. Zheng, H.F. Cheng, *CrystEngComm* 14 (2012) 1687–1692.
- [32] Z.H. Sun, J.J. Guo, S.M. Zhu, L. Mao, J. Ma, D. Zhang, *Nanoscale* 6 (2014) 2186–2193.
- [33] K. Pingmuang, A. Nattestad, W. Kangwansupamonkon, G.G. Wallace, S. Phanichphant, J. Chen, *Appl. Mater. Today* 1 (2015) 67–73.
- [34] J. Xu, W.Z. Wang, J. Wang, Y.J. Liang, *Appl. Surf. Sci.* 349 (2015) 529–537.
- [35] S.D. Perera, R.G. Mariano, K. Vu, N. Nour, O. Seitz, Y. Chabal, K.J. Balkus, *ACS Catal.* 2 (2012) 949–956.
- [36] E. Gao, W.Z. Wang, M. Shang, J.H. Xu, *Phys. Chem. Chem. Phys.* 13 (2011) 2887–2893.
- [37] M. Wang, Q. Liu, Y.S. Che, L.F. Zhag, D. Zhang, *J. Alloys Compd.* 548 (2013) 70–76.
- [38] P. Madhusudan, J.R. Ran, J. Zhang, J.G. Yu, G. Liu, *Appl. Catal. B: Environ.* 110 (2011) 286–295.
- [39] H.Z. Zhao, X.L. Chen, C.C. Jia, T. Zhou, X.H. Qu, J.K. Jian, Y.P. Xu, T. Zhou, *Mater. Sci. Eng. B* 122 (2005) 90–93.
- [40] P. Periyat, K.V. Baiju, P. Mukundan, P.K. Pillai, K.G.K. Warrier, *Appl. Catal. A: Gen.* 349 (2008) 13–19.
- [41] S.M. Thalluri, M. Hussain, G. Saracco, J. Barber, N. Russo, *Ind. Eng. Chem. Res.* 53 (2014) 2640–2646.
- [42] X.M. Dang, X.F. Zhang, Z.Y. Lu, Z.Z. Yang, X.L. Dong, X.X. Zhang, C. Ma, H.C. Ma, M. Xue, F. Shi, *J. Nanopart. Res.* 16 (2) (2014) 839–843.
- [43] H.Y. Nie, M. Ou, Q. Zhong, S.L. Zhang, L.M. Yu, *J. Hazard. Mater.* 300 (2015) 598–606.
- [44] W. Liu, M.L. Wang, C.X. Xu, S.F. Chen, *Chem. Eng. J.* 209 (2012) 386–393.
- [45] L.Q. Ye, J.Y. Liu, Z. Jiang, T.Y. Peng, L. Zan, *Appl. Catal. B: Environ.* 142–143 (2013) 1–7.
- [46] H.Y. Nie, M. Ou, Q. Zhong, S.L. Zhang, L.M. Yu, *J. Hazard. Mater.* 300 (2015) 598–606.